Delft University of Technology

Stopping Voltage-Dependent PCM and RRAM-Based Neuromorphic Characteristics of Germanium Telluride

Abbas, Yawar; Ansari, Sumayya M.; Taha, Inas; Abunahla, Heba; Khan, Muhammad Umair; Rezeq, Moh'd; Aldosari, Haila M.; Mohammad, Baker

DOI
10.1002/adfm.202214615

Publication date
2023

Document Version
Final published version

Published in
Advanced Functional Materials

Citation (APA)
Abbas, Y., Ansari, S. M., Taha, I., Abunahla, H., Khan, M. U., Rezeq, M., Aldosari, H. M., & Mohammad, B. (2023). Stopping Voltage-Dependent PCM and RRAM-Based Neuromorphic Characteristics of Germanium Telluride. *Advanced Functional Materials*, *34*(15), Article 2214615. https://doi.org/10.1002/adfm.202214615

Important note
To cite this publication, please use the final published version (if applicable).
Please check the document version above.

Copyright
Other than for strictly personal use, it is not permitted to download, forward or distribute the text or part of it, without the consent of the author(s) and/or copyright holder(s), unless the work is under an open content license such as Creative Commons.

Takedown policy
Please contact us and provide details if you believe this document breaches copyrights.
We will remove access to the work immediately and investigate your claim.

This work is downloaded from Delft University of Technology.
For technical reasons the number of authors shown on this cover page is limited to a maximum of 10.

Exploring the possibilities of increasing energy density and efficiency in rechargeable batteries

Download this complimentary article collection

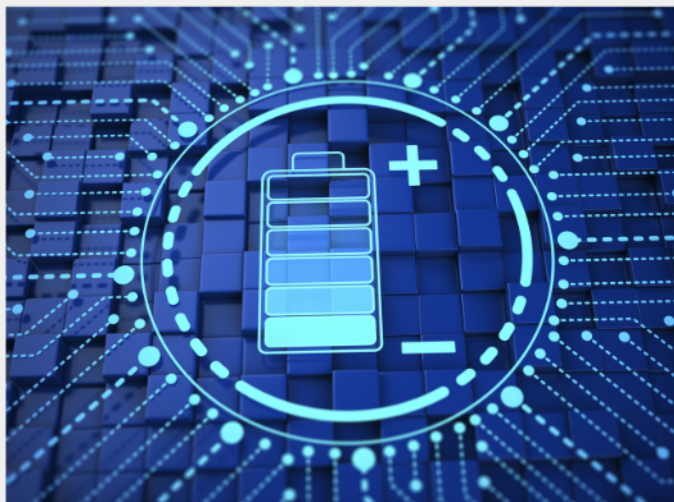

The exponential rise in the need for better, more efficient power sources has sparked an incredible amount of research into batteries. A primary focus of research has been increasing the energy density of batteries, as it allows for lighter, more portable storage of energy. Lithium-ion batteries, for example, have a much higher energy density than conventional lead-acid batteries and can be used for various purposes, such as in electric vehicles.

This article collection provides a comprehensive list of references for new methods and technologies for increasing the energy density of batteries.

WILEY

ADVANCED FUNCTIONAL MATERIALS
www.afm-journal.de

Check for updates

Stopping Voltage-Dependent PCM and RRAM-Based Neuromorphic Characteristics of Germanium Telluride

Yawar Abbas, Sumayya M. Ansari, Inas Taha, Heba Abunahla, Muhammad Umair Khan, Moh'd Rezeq, Haila M. Aldosari, and Baker Mohammad**

Recently, phase change chalcogenides, such as monochalcogenides, are reported as switching materials for conduction-bridge-based memristors. However, the switching mechanism focused on the formation and rupture of an Ag filament during the SET and RESET, neglecting the contributions of the phase change phenomenon and the distribution and re-distribution of germanium vacancies defects. The different thicknesses of germanium telluride (GeTe)-based Ag/GeTe/Pt devices are investigated and the effectiveness of phase loops and defect loops future application in neuromorphic computing are explored. GeTe-based devices with thicknesses of 70, 100, and 200 nm, are fabricated and their electrical characteristics are investigated. Highly reproducible phase change and defect-based characteristics for a 100 nm-thick GeTe device are obtained. However, 70 and 200 nm-thick devices are unfavorable for the reliable memory characteristics. Upon further analysis of the Ag/GeTe/Pt device with 100 nm of GeTe, it is discovered that a state-of-the-art dependency of phase loops and defect loops exists on the starting and stopping voltage sweeps applied on the top Ag electrode. These findings allow for a deeper understanding of the switching mechanism of monochalcogenide-based conduction-bridge memristors.

Y. Abbas, M. Rezeq
Department of Physics
Khalifa University
Abu Dhabi 127788, United Arab Emirates

Y. Abbas, H. Abunahla, M. U. Khan, M. Rezeq, B. Mohammad
System on Chip Lab
Khalifa University
Abu Dhabi 127788, United Arab Emirates
E-mail: baker.mohammad@ku.ac.ae

S. M. Ansari, I. Taha, H. M. Aldosari
Department of Physics
United Arab Emirates University
Al Ain 15551, United Arab Emirates
E-mail: haldosari@uaeu.ac.ae

H. Abunahla, M. U. Khan, B. Mohammad
Department of Electrical Engineering and Computer Science
Khalifa University
Abu Dhabi 127788, United Arab Emirates

H. Abunahla
Quantum and Computer Engineering Department
Delft University of Technology
Delft 5058, Netherlands

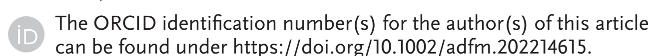
The ORCID identification number(s) for the author(s) of this article can be found under https://doi.org/10.1002/adfm.202214615.

© 2023 The Authors. Advanced Functional Materials published by Wiley-VCH GmbH. This is an open access article under the terms of the Creative Commons Attribution License, which permits use, distribution and reproduction in any medium, provided the original work is properly cited.

DOI: 10.1002/adfm.202214615

1. Introduction

Due to excessive power consumption caused by unexpected leakage currents, transistors approach their ultimate limits of miniaturization.[1] This power consumption issue has been addressed by the fabrication of devices with low voltage supplies, such as tri-gate gate field effect transistors (FET),[2] negative capacitance FET,[3] tunnel FET,[4] and non-charge-based devices.[5] Additionally, the Von Neumann bottleneck has been addressed by the 3D integration of computing and memory elements or by introducing new architecture, such as in-memory logic[6] and neuromorphic computing.[7] Furthermore, phase change memory (PCM)[8] and resistive switching memory (RRAM)[9] have successfully demonstrated their candidacy to serve as simultaneous memory and computing elements.[10]

The state of PCM and RRAM devices can be modulated by applying an external electric stress by changing the phase and resistance of the device, respectively. Specific device resistances and phase tuning are achieved by applying different stopping voltages and appropriate pulse parameters. With the help of externally applied stimulations, PCM and RRAM have successfully demonstrated synaptic element capability due to their ability to resistance tuning.[11] However, the application of PCM and RRAM devices as reliable memory elements and neurons for neuromorphic hardware requires the optimization of specific properties, such as thickness, structural engineering, interface behaviors, and material selections.

Chalcogenides are compounds consisting of tellurium (Te), selenium (Se), and sulfur (S) with exceptional electronic, optical, magnetic, and thermal properties.[12] Among all chalcogenides, the Te-containing phase change chalcogenides have amorphous or glassy phases which can undergo fast crystallization.[13] Although the short crystallization time is challenging to measure, reversible amorphous-to-crystallization transitions are critical processes in erasing, i.e., amorphization and writing, i.e., crystallization in PCM operations.

Germanium telluride (GeTe) is emerging as an excellent switching material with memory characteristics and neuromorphic applications. Recently, Yu et al.[14] determined the non-volatile and typical selector characteristics of Ag/Ag–GeTe/Ag devices by changing the atomic ratio of Te with

a controlled co-sputtering technique. Li et al.[15] reported a bilayer memristor, with a $Pt/Cu/GeTe/Al_2O_3/Pt$ stacking structure, demonstrating the gradual SET and RESET processes for the optimized 3 nm-thick Al_2O_3 layer. The device exhibited threshold switching for the 5 and 7 nm-thick Al_2O_3 layers. The laterally fabricated GeTe-based PCM device based was also reported to achieve multilevel resistance states.[16] Direct current (DC) sweeps and rectangular pulse-mode low voltages were used to obtain these multilevel resistance states. In these reports, the conduction mechanism focuses on the migration of active ions (i.e., Ag^+ or Cu^{+2}) when the voltages are applied on the device, neglecting the phase changes and contribution of germanium vacancies (V_{Ge}). No report has focused on the thickness-dependent PCM and RRAM characteristics of GeTe-based devices for their potential application in neuromorphic computing.

In this study, we optimized the thickness of Ag/GeTe/Pt-based devices for the bifunctional memory characteristics, including PCM and analog-type resistive switching. Different thicknesses of GeTe thin films were analyzed to investigate their suitability for neuromorphic applications. The results revealed that the device's PCM and analog switching characteristics depended on the initial voltage values and stopping voltages. The high-resolution transmission electron microscopy (HRTEM) analysis of the device in different switching states confirmed the Ag migration and phase change in the devices. Furthermore, the potentiation and depression characteristics confirmed that GeTe-based devices exhibited better neuromorphic characteristics in the phase mode compared to that of the defect switching mode. The accuracy of the phase change and RRAM were calculated as 86% and 65%, respectively. This research will provide a new method for better understanding the switching mechanics in Ag/GeTe/Pt-based devices.

2. Results and Discussion

Figure 1 shows a schematic of the fabrication flow of Ag/GeTe/Pt/Ti/SiO_2 and its physical characteristics. Figure 1a shows the device fabrication and its potential application in artificial synapses. Figure 1b shows the complete process of lamella extraction using a focused ion beam (FIB) from the device under test for further analysis in the HRTEM. After removing the lamella with the help of an Omniprobe, it was attached to the Cu grid for the HRTEM analysis. Figure 1c shows the complete device with a stacking sequence of Ag/GeTe/Pt with a 100 nm-thick layer of GeTe. Furthermore, we performed cross-sectional measurements on GeTe-based devices with 70 and

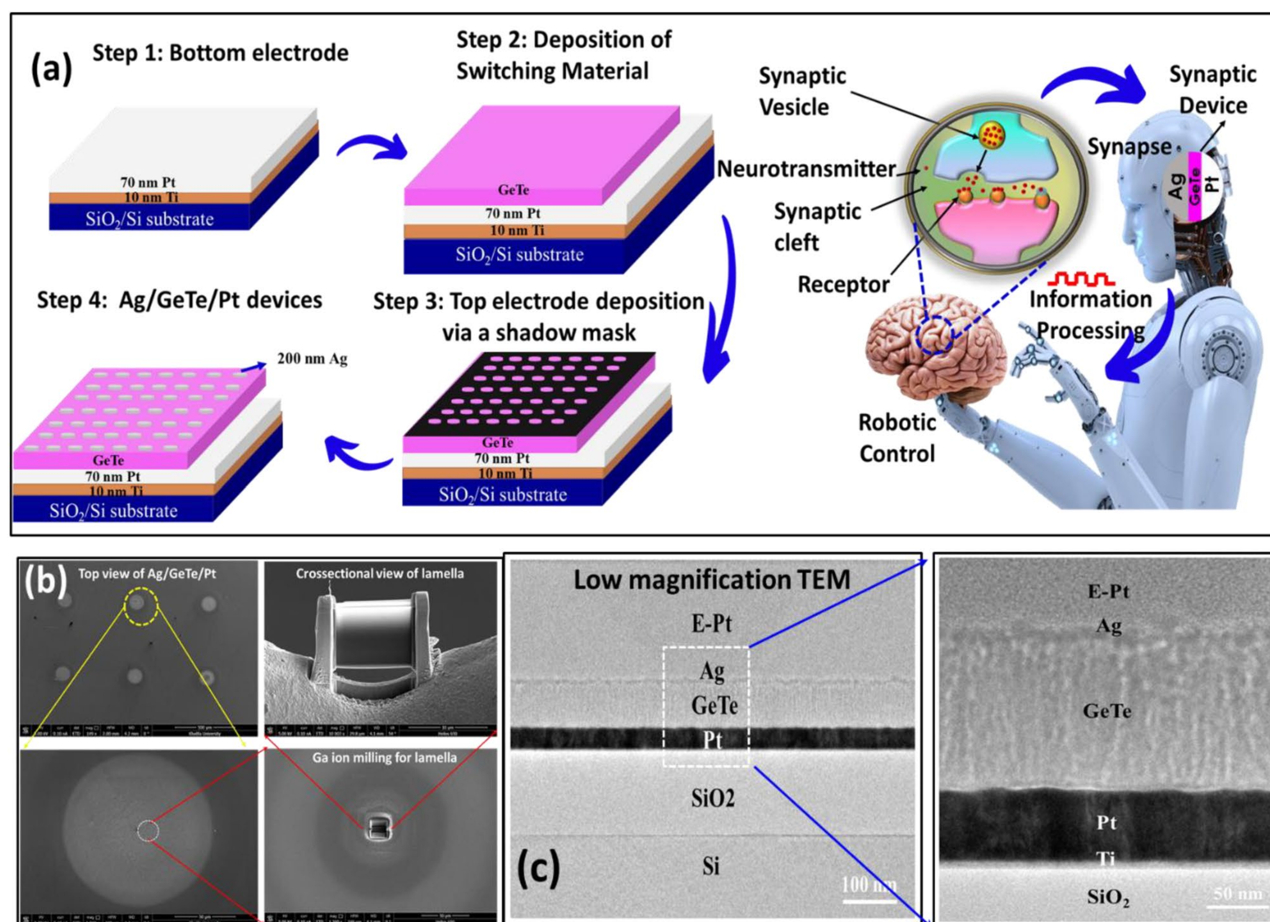

Figure 1. a) Schematic of the device fabrication and its application as a synaptic device, b) the top view of the Ag/GeTe/Pt device and its lamella for the HRTEM analysis, and c) the cross-sectional low- and high-magnification HRTEM images of the device.

© 2023 The Authors. Advanced Functional Materials published by Wiley-VCH GmbH

16163028, 0, Downloaded from https://onlinelibrary.wiley.com/doi/10.1002/adfm.202214615 by Tu Delft, Wiley Online Library on [01/05/2023]. See the Terms and Conditions (https://onlinelibrary.wiley.com/terms-and-conditions) on Wiley Online Library for rules of use; OA articles are governed by the applicable Creative Commons License

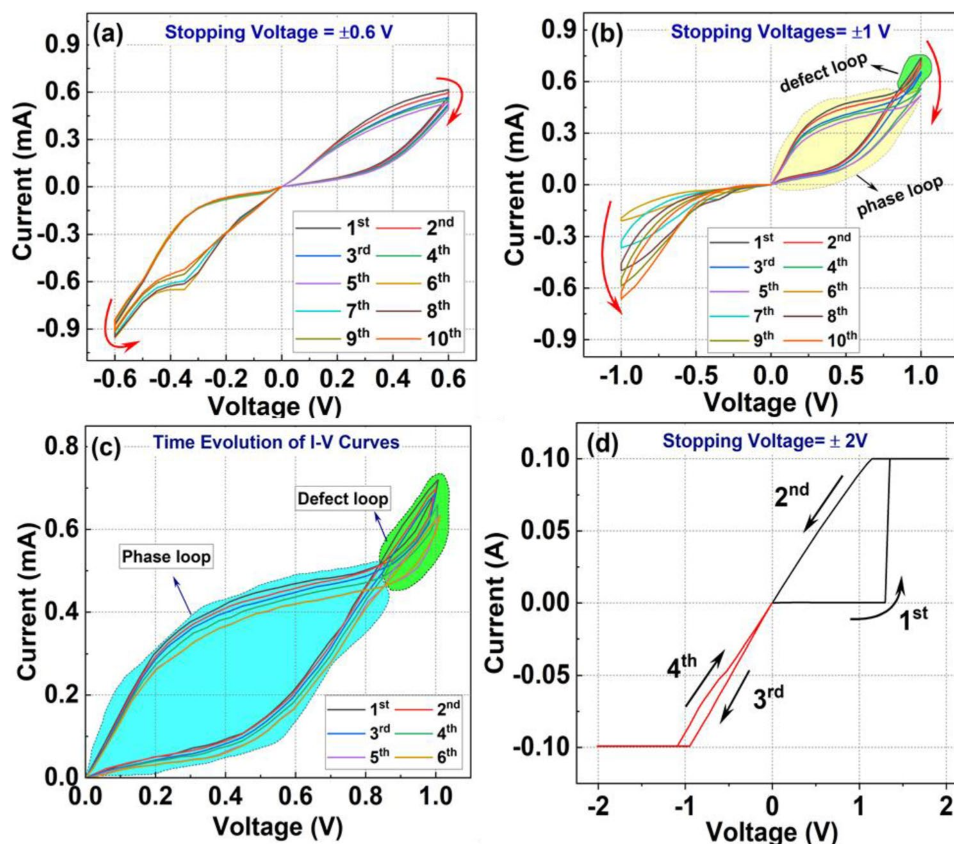

Figure 2. Typical *I–V* characteristics of an Ag/GeTe/Pt-based device depicting a) the electrical characteristics for a ± 0.6 V stopping voltage, b) the SET and RESET process for the stopping voltage of ± 1.0 V, c) the time evolution of *I–V* sweeps, and d) the high voltage permanent breakdown of the device.

200 nm-thick layers of GeTe, as shown in Figure S1 (Supporting Information).

Figure 1c presents the low- and high-magnification, bright-field, cross-sectional transmission electron microscopy (TEM) images of the as-deposited device before conducting any electrical measurements. The images reveal that the top layer of the Ag electrode completely diffused into the GeTe thin film and created an alloy, which is consistent with the results from Cooley et al.[17] Pristine GeTe thin films that are deposited at room temperature are amorphous.[18] However, upon Ag diffusion, the crystallinity of the films improved, as evident from the faint scattered fringes.

The initial test for the device's suitability was performed by investigating the electrical characteristics and observing the device's dependency on the stopping voltages. **Figure 2** shows the Current–voltage (*I–V*) characteristics of the 100 nm-thick GeTe-based devices for different stopping voltage values, ± 0.6, ± 1, and ± 2 V, with and without introducing relaxation time. Figure 2a depicts the successive *I–V* loops at the stopping voltage sweeps of ± 0.6 V. The overall resistance of the devices increased when positive sweeps were applied and decreased when negative sweeps were applied, forming a single loop. This single loop, which we define as the "phase loop", formed due to the amorphous-to-crystalline phase transition of the GeTe. The gradual change in resistance occurred after consecutive sweeps, implying that the Ag/GeTe/Pt device was suitable for neuromorphic hardware applications.[19]

Extending the stopping voltage value to ± 1 V resulted in the appearance of an additional, small loop, as shown in Figure 2b. The formation of this loop is attributed to the accumulation of germanium defects (V_{Ge}), as it vanishes with consecutive sweeps. Thus, this loop was defined as the "defect loop". The accumulation of these vacancies creates volatile nanochannels within the switching medium.[20] The application of consecutive voltage sweeps aligned all the vacancies, which resulted in the loss of the defect loop for the additional sweeps. To confirm the volatility of the phase loop and defect loop, the time evolution electrical characteristics were performed with every *I–V* taken after a waiting time of 10 min, as shown in Figure 2c. The overall resistance of the device was observed to increase with each sweep, but the defect loop was maintained, as shown in the highlighted region of Figure 2c. The appearance of the defect loop after each sweep for the waiting time of 10 min was attributed to the re-distribution and accumulation of V_{Ge}[21] within the GeTe thin film during the sweep.[22]

To investigate the effect of a high stopping voltage on the electrical characteristics of the device, we applied a stopping voltage of ± 2.0 V, as shown in Figure 2d. A permanent breakdown was observed at this high voltage, rendering the device into a Write Once Read Many (WORM) device. This permanent breakdown was caused by the formation of Ag-based nano-island, and permanent crystalline formation of GeTe and γ-AgGeTe phases, which will be elaborated later in the TEM analysis. Figure 2a,b shows that different loops appear for

© 2023 The Authors. Advanced Functional Materials published by Wiley-VCH GmbH
16163028, 0, Downloaded from https://onlinelibrary.wiley.com/doi/10.1002/adfm.202214615 by Tu Delft, Wiley Online Library on [01/05/2023]. See the Terms and Conditions (https://onlinelibrary.wiley.com/terms-and-conditions) on Wiley Online Library for rules of use; OA articles are governed by the applicable Creative Commons License

16163028, 0, Downloaded from https://onlinelibrary.wiley.com/doi/10.1002/adfm.202214615 by Tu Delft, Wiley Online Library on [01/05/2023]. See the Terms and Conditions (https://onlinelibrary.wiley.com/terms-and-conditions) on Wiley Online Library for rules of use; OA articles are governed by the applicable Creative Commons License

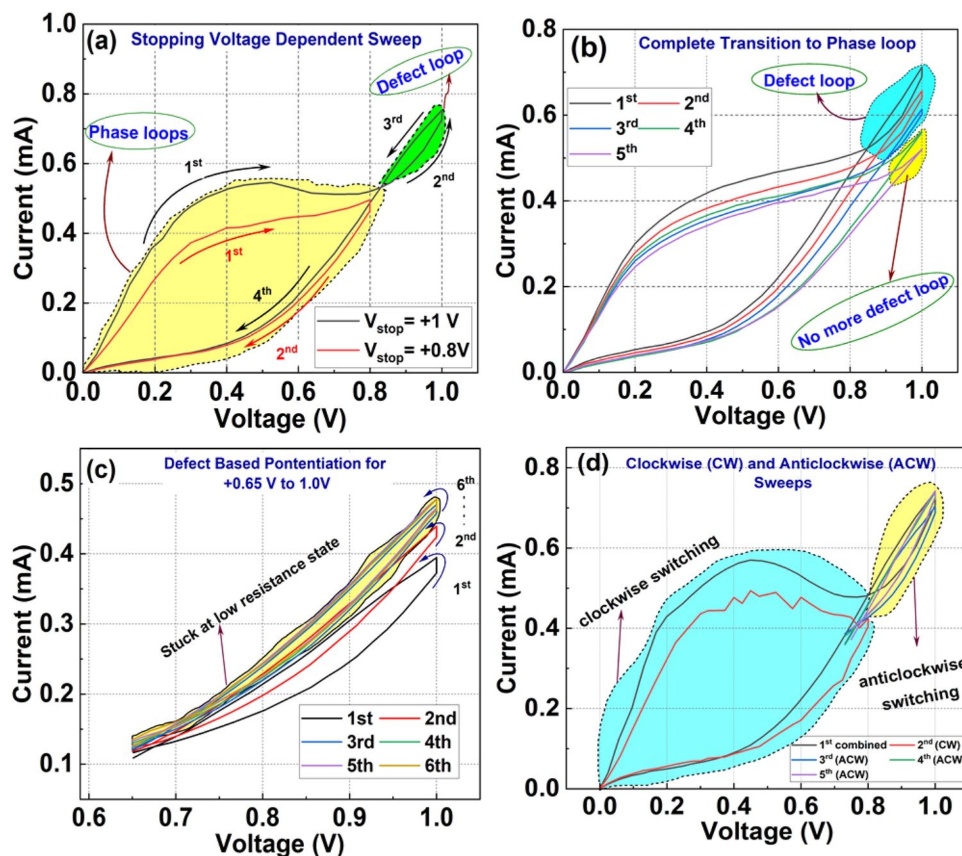

Figure 3. Initial and stopping voltage-dependent switching: a) the electrical characteristics of stopping voltages + 0.8 and + 1.0 V, b) the consecutive sweep at a stopping voltage of + 1.0 V to eliminate the defect loop, c) the consecutive *I–V* loops at the initial and stopping voltages of + 0.65 and + 1.0 V, respectively, and d) the voltage-dependent transition from the phase to defect loop, and vice versa.

different stopping voltages. At high voltages (≈0.65 to +1.0 V), the loops are categorized as (V_{Ge})-based switching. At low voltages (0 to +0.65 V), the loops are categorized as phase change phenomena. By applying a complete sweep loop from 0 to +1 V to 0 and 0 to –1 V to 0, phase loops and defect loops activate. The phase loops had bigger memory windows compared to those of the defect loops, resulting in the SET and RESET processes. Therefore, the resistance of the device decreases for negative sweeps and increases for positive sweeps.

The stopping voltage and thickness-dependent switching characteristics were investigated for 70 and 200 nm-thick GeTe-based devices, as depicted in Figure S2 (Supporting Information). After comparing the electrical characteristics of Figure 2 with Figure S2 (Supporting Information), it is evident that 100 nm was the optimum thickness for further investigations of neuromorphic characteristics. The 100 nm-thick GeTe thin films were chosen as they showed great performance and device-to-device reproducibility compared to the 70 and 200 nm-thick films.

To further understand the switching characteristics presented by the devices shown in Figure 2, the electrical characteristics were performed at different starting and stopping voltages, as shown in **Figure 3**. Figure 3a shows the stopping voltage-dependent electrical characteristics of the device at the stopping voltages of + 0.8 and + 1.0 V. For the stopping of + 0.8 V, there was only one *I–V* loop in the clockwise (CW) direction. However, in the case of the + 1.0 V sweep, we observed two different loops and have labeled the directions of the sweeps with arrows. The yellow highlighted loop, in the CW direction, is dedicated to the phase change in GeTe. In contrast, the green highlighted loop, in the anticlockwise (ACW) direction, is dedicated to the contribution from the V_{Ge} in GeTe.

The essential characteristic, i.e., the elimination of the defect loop, was observed when multiple consecutive sweeps were performed on the device, as shown in Figure 3b. It is well-established that the device will go into a temporary non-switching state for the analog switching memristors when all defects accumulate.[23] Therefore, it was essential to notice the defect loop disappearance after the 3rd sweep. For analog switching memristors, the conductance of the device changes according to the application of consecutive voltage sweeps and their polarity.[20c] Once the device reaches its maximum conductance for the set process and minimum conductance for the reset process (depending on the polarity), it temporarily stays in that state due to the maximum alignment of the defects. Hence, the loop disappears.[24] In Figure 3b, after the application of the 3rd voltage sweep, we observed that the defect loop was eliminated because of the maximum alignment of V_{Ge}.

To further validate the effect of starting and stopping voltages on the electrical characteristics, the *I–V* loops were

© 2023 The Authors. Advanced Functional Materials published by Wiley-VCH GmbH

16163028, 0, Downloaded from https://onlinelibrary.wiley.com/doi/10.1002/adfm.202214615 by Tu Delft, Wiley Online Library on [01/05/2023]. See the Terms and Conditions (https://onlinelibrary.wiley.com/terms-and-conditions) on Wiley Online Library for rules of use; OA articles are governed by the applicable Creative Commons License

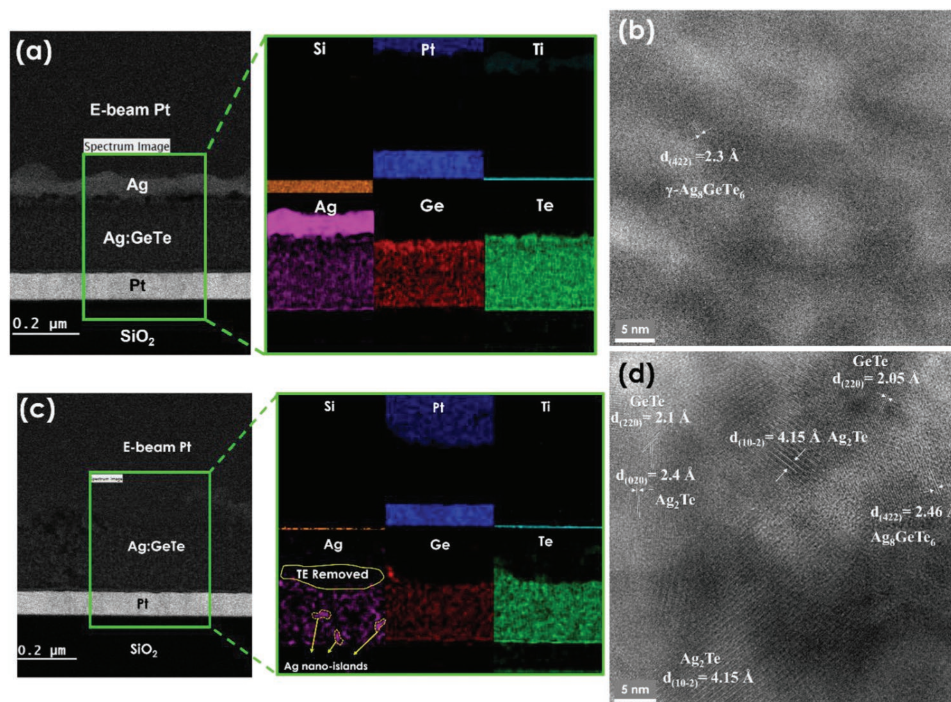

Figure 4. Systematics of the structural impact of the stopping voltage and corresponding switching mechanism. a) Cross-sectional STEM image of the device, after 5 cycles, using a stopping voltage of ± 1 V with EELS elemental mapping images for the green rectangular region, b) Its corresponding structural impact, c) Cross-sectional STEM image of the device after using a breakdown voltage of 2 V with EELS elemental mapping images for the green rectangular region, and d) Its corresponding structural impact.

carried from + 0.65 to + 1.0 V, and back to + 0.65 V, as shown in Figure 3c. Interestingly, we only detected the defect loop in the ACW direction, and the overall resistance of the device decreased. Thus, the complete transition from defect loop to phase loop, and vice versa, was demonstrated by controlling the initial and stopping voltages in the ACW and CW directions, as depicted in Figure 3d. From the results of Figure 3, it can be inferred that the 100 nm-thick GeTe-based device exhibits PCM and RRAM characteristics, depending on the application of an initial and stopping voltage on the top Ag electrode.

To investigate the effect of applied voltage on the structural properties of the device, we performed a TEM analysis on the device after low voltage sweeps and the breakdown state. From the results, we proposed a switching mechanism based on the TEM analysis, as shown in **Figure 4**. Figure 4a shows the cross-sectional TEM image and its corresponding electron energy loss spectroscopy (EELS) elemental mapping of the device after the low voltage sweeps. Notably, Ag diffused into the GeTe film without prior application of an electric bias. Hence, in the pristine state, the switching medium can be considered as Ag-doped GeTe, also known as Ag:GeTe, which has been previously reported in literature.[14] Figure 4b shows the magnified image of the switching medium depicting the amorphous nature of Ag:GeTe.[18] Figure 4a reveals that half of the top layer of the Ag electrode diffused into the GeTe thin film. Although pristine GeTe thin films that are deposited at room temperature are amorphous,[18] the crystallinity of the films improved upon Ag diffusion, as evident from the faint scattered fringes shown in Figure 4b.

The device was further analyzed in TEM after applying a high breakdown voltage of + 2.0 V, as shown in Figure 4c,d. EELS elemental mapping of the device's cross-section showed that the top Ag electrode was completely removed from the top of the device and prominent nano-island formations were observed in the switching Ag:GeTe layer, as shown in Figure 4c. The crystallinity of the switching layer improved upon the increase in the stopping voltage value, as seen in Figure 4b,d. EELS elemental mapping and interplanar spacing calculations suggest the formation of Ag_2Te (monoclinic crystal structure, space group $P12_1/c1$) and γ-Ag_8GeTe_6 (cubic crystal structure, space group $F4$-$3m$) within the rhombohedral GeTe (space group: $R3m$) matrix. As seen from the EELS maps, the localization of Ag nano-islands supported Ag filament formation within the switching layer. In Figure 4b, the lattice fringe was spaced by 2.3 Å, which corresponds to the (422) plane of the γ-Ag_8GeTe_6 phase. In Figure 4d, the lattice fringes were spaced by 2.83 and 2.05 Å, which correspond to the (422) and (220) planes of the γ-Ag_8GeTe_6 and GeTe phases, respectively. The lattice fringes spaced by 2.4 and 4.15 Å correspond to the (020) and (102) planes of the Ag_2Te intermetallic phase, respectively. These crystallizations were caused by the joule-heating effect, which has been widely accepted in literature.[25]

Figure S3 (Supporting Information) shows the detailed structural transformation within the switching medium and at the interfaces for the pristine device, a device after low voltage, and a device after the application of high voltage. The TEM images of the pristine device, switching device, and high voltage breakdown device, clearly show the amorphous, less crystalline, and highly crystalline structures, respectively, in the

 © 2023 The Authors. Advanced Functional Materials published by Wiley-VCH GmbH

16163028, 0, Downloaded from https://onlinelibrary.wiley.com/doi/10.1002/adfm.202214615 by Tu Delft, Wiley Online Library on [01/05/2023]. See the Terms and Conditions (https://onlinelibrary.wiley.com/terms-and-conditions) on Wiley Online Library for rules of use; OA articles are governed by the applicable Creative Commons License

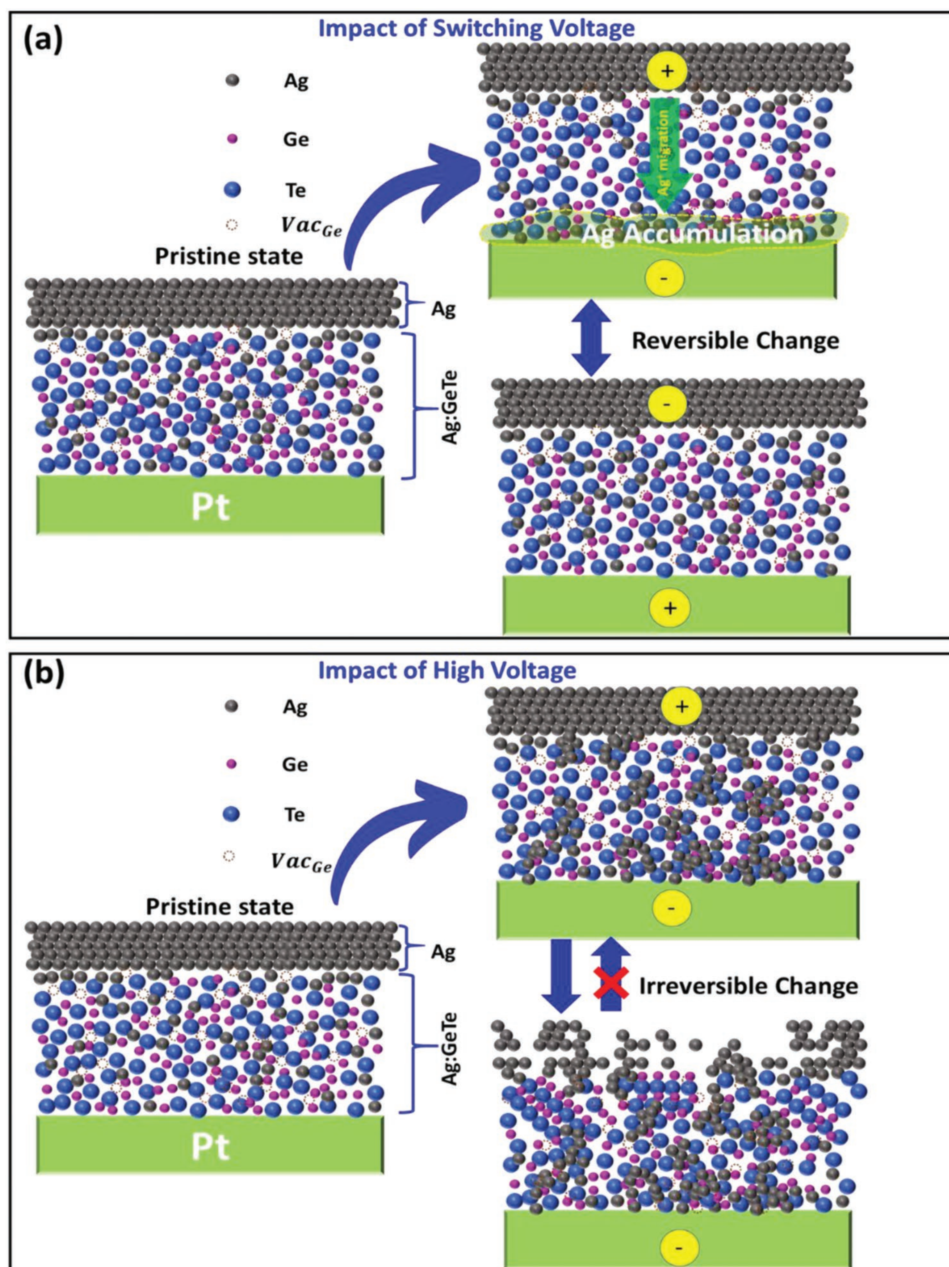

Figure 5. The proposed switching mechanism for a) the low stopping voltage and b) the high stopping voltage.

switching medium upon the application of different stopping voltages. Furthermore, the crystalline planes directly related to the GeTe and γ-AgGeTe phases after low and high stopping voltages confirms the phase change behavior of the devices. These TEM analyses are direct proof that phase changes occur in the device upon the application of voltages.

Based on the TEM images, the complete switching phenomenon observed in Figures 2 and 3 is schematically explained in **Figure 5**. Figure 5a shows the change in resistance when the voltages were applied to the top Ag electrode. Since Ag already existed in the switching medium, the application of a positive bias on the top electrode caused additional Ag migration toward the GeTe/Pt interface. This resulted in the decrease of Ag concentration in the switching medium, which caused an increase in the resistance with each sweep. After the application of a low negative stopping voltage sweep, the accumulated Ag diffused back into the GeTe layer, forming the Ag:GeTe switching medium. Thus, the process is reversible for low stopping voltages of $\leq \pm 1.0$ V. For the high stopping voltage of ± 2.0 V, the diffused Ag and Ag from the top electrode migrated into the GeTe film. During this migration, the Ag accumulated in the GeTe film, creating a connected nanoscale island-based, permanent film and permanently damaged the top electrode, as shown in Figure 5b. The damage to the top electrode was further confirmed using the top view scamming electron microscope (SEM) micrograph of the hard breakdown devices, as

© 2023 The Authors. Advanced Functional Materials published by Wiley-VCH GmbH

shown in Figure S4 (Supporting Information). We believe the Ag migration obeys the following redox reaction during the switching phenomenon, which has been widely accepted in the research community.[26]

$$Ag \rightarrow Ag^{+} + 1e^{-} \quad \text{Oxidation} \tag{1}$$

$$Ag^{+} + 1e^{-} \rightarrow Ag \quad \text{Reduction} \tag{2}$$

To further elucidate the electrical characteristics, the contribution of the germanium defects or vacancies should be addressed as the *p*-type conduction of GeTe owing to the high concentration of germanium vacancies or defects.[27] When the bias voltage was applied to the devices, the electric field forced these defects to re-distribute in the GeTe film, resulting in the annihilation of unfavorable anti-bonding Ge–Te and Ag–Te interactions.[27b] Hence, the number of free electrons available for the conduction was sufficiently reduced. This drove the device's transition from a low resistance to a high resistance.[28]

The phase and defect memory states of the GeTe device were evaluated with neuromorphic computation in **Figure 6**. Data were acquired with a sophisticated pulse scheme to mimic the spike rate-dependent plasticity (SRDP). This method applied repetitive pulses with amplitudes of 0.4, 0.5, and 0.6 V, and kept a pulse width of 1 ms, as shown in Figure 6a. The paired-pulse depression (PPD) of the device was observed with the rate of change of resistance, i.e., $(R_2 - R_1)/R_1$, as shown in Figure 6b. The voltage of 0.6 V had a lower PPD value than that of 0.4 V. Similarly, the synaptic weight varied gradually with the different pulse amplitudes, which corresponded with the gradual change

Figure 6. a) Plasticity characteristics with different pulse amplitudes of 0.4, 0.5, and 0.6 V, by keeping the pulse at 1 ms. b) The pulse pair depression behavior of the device was calculated from different pulse amplitudes. c) The artificial synapse response at various pulse widths: 1, 2, and 3 ms. d) Potentiation and depression of the phase and defect regions. Normalized weight of the e) phase and f) defects regions. g) CNN for recognition of the CIFAR-10 data set. h) Simulated accuracies of the phase and defect regions of the GeTe neuromorphic device.

© 2023 The Authors. Advanced Functional Materials published by Wiley-VCH GmbH

16163028, 0, Downloaded from https://onlinelibrary.wiley.com/doi/10.1002/adfm.202214615 by Tu Delft, Wiley Online Library on [01/05/2023]. See the Terms and Conditions (https://onlinelibrary.wiley.com/terms-and-conditions) on Wiley Online Library for rules of use; OA articles are governed by the applicable Creative Commons License

in the device resistance. The synaptic weight of the GeTe artificial synapse device could be controlled by externally delivered pulses with varying pulse width schemes. Pulse widths of 1, 2, and 3 ms, were studied by applying the sequential synaptic pulses with an amplitude of 0.4 V, as shown in Figure 6c.

From the weight change data set of the phase and defect behaviors, we obtained the simulation parameters for a convolutional neural network (CNN) that could be used to evaluate the proposed device's performance.[29] As shown in Figure 6d, the weight change behaviors of the phase and defect regions were obtained by applying a continuous 500 pulse train for potentiation and depression, respectively, with a pulse width of 1 ms. As seen from Figures 2 and 3, it is clear that the phase loops are more prominent than the defect loops and the device follows the CW loop for the PCM characteristics. Therefore, the improved resistances of the devices were observed after the application of voltage pulses of amplitude 0.4, 0.5, and 0.6 V, by keeping a pulse width of 1 ms. The potentiation and depression of the phase loops were performed by using ± 0.3 V with a pulse width of 1 ms. The potentiation and depression of the defect loop were carried out at ± 0.7 V with a pulse width of 1 m and 500 potentiation and 500 depression pulses.

In NeuroSim, the nonlinearity of the weight update can be computed from Equations 3, 4, and 5:[29,30]

$$G_{\mathrm{LTP}} = B\left(1 - e^{-\frac{P}{A}}\right) + G_{\min} \tag{3}$$

$$G_{\mathrm{LTD}} = -B\left(1 - e^{-\frac{P - P_{\max}}{A}}\right) + G_{\max} \tag{4}$$

$$B = \left(G_{\max} - G_{\min}\right) / \left(1 - e^{\frac{-P_{\max}}{A}}\right) \tag{5}$$

In these equations, P is the pulse number at which the conductance changed, G_{LTP} is the weight change for potentiation, G_{LTD} denotes the weight values for depression, $G_{\max}$ and $G_{\min}$ are the maximum conductance and minimum conductance, respectively, $P_{\max}$ is the maximum number of pulses necessary to switch the device between the lowest and highest conductance levels, and A controls the nonlinear nature of weight updating.

The nonlinearity value can be calculated using the Generalized Simulated Annealing (GSA) algorithm using MATLAB. The maximum and minimum conductance of the device in the phase state were 121 and 476.7 µS, respectively, with an OFF/ON ratio of ≈2.55. The nonlinearities for positive and negative pulse data were 1.9 and 2.48, respectively, as shown in Figure 6e. The maximum and minimum conductance for the device in the defect state were 504.7 and 404.4 µS, respectively, with an OFF/ON ratio of ≈1.24. The nonlinearities for the potentiation and depression pulse data were 1.95 and 5.85, respectively, as shown in Figure 6f. We used CIFAR-10 recognition data for the CNN simulation and the input was 32 × 32 × 3.

In this study, six convolutional layers were used to extract features, and the last two fully connected layers were used to classify those features, as shown in Figure 6g. In the Figures S5 and S6 (Supporting Information), we discussed our parallel-readout, eNVM-based, pseudo-crossbar pursuit device array method and hardware implementation of the CNN.[29,30] As shown in Figure 6h, we have simulation results for the comparison of a phase and defect region. The phase region presented the maximum accuracy compared to that of the defect region. In 200 epochs, the accuracy of the neural networks for the phase and defect regions were 86% and 65%, respectively. The phase region converged to a higher accuracy than that of the defect region because of its greater OFF/ON ratio and lower nonlinearity values for pentation and depression.

3. Conclusion

In summary, we investigated the different thicknesses of GeTe-based monochalcogenide for its application in neuromorphic hardware. The Ag/GeTe/Pt device with a 100 nm-thick GeTe layer exhibited unprecedented initial voltage- and stopping voltage-dependent *I–V* characteristics. For the double voltage sweeps of 0 to ± 0.6 V to 0, 0 to ± 1.0 V to 0, and + 0.6 to + 1 to + 0.6 V, the phase change base, a mixture of phase- and vacancy-based, and vacancy-based switching were observed, respectively. They acted as WORM devices and severe damage to the top Ag electrode was observed after the high voltage sweeps of 0 to ± 2.0 V to 0. The structural impact of stopping voltages was further analyzed with the help of cross-sectional TEM. Prominent phase change and Ag migration inside the GeTe film were observed. Finally, the switching mechanisms of the devices were discussed with the help of Ag-migration and the accumulation of germanium vacancies and defects upon application of the electric field. From the potentiation and depression characteristics at different switching modes, it is concluded that PCM characteristics in Ag/GeTe/Pt are much more favorable for neuromorphic applications, with 86% accuracy.

4. Experimental Section

Amorphous GeTe thin films, acting as the switching layer, with thicknesses of 70, 100, and 200 nm, were deposited on commercially available Pt/Ti/SiO_2 substrates using DC magnetron sputtering of a 99.999% pure stoichiometric GeTe target. Seventy nanometer-thick Pt was appointed as the bottom electrode and 10 nm-thick Ti was set as a buffer layer to improve the adhesion between the Pt and SiO_2 layers. Then, 200 nm-thick Ag was established as the top electrode. It was deposited on the GeTe thin films using DC magnetron sputtering of a 99.999% pure Ag target through a 100 µm diameter circular-shaped shadow mask. The applied DC sputtering powers were 37 and 35 W for GeTe and Ag, respectively, obtaining a deposition rate of ≈1 Å s^{-1}. The samples were rotated at 15 rpm during deposition, ensuring film uniformity. Ar gas was used as the sputter gas and introduced into the chamber at a fixed flowrate of 25 sccm, resulting in a working pressure of 7.9×10^{-1} Pa. All fabrication steps were performed at room temperature, making the device compatible with complementary metal–oxide–semiconductor technologies. *I–V* characteristics were performed using a Keithley 4200A semiconductor parameter analyzer and applying appropriate voltage sweeps on the top Ag electrode. The bottom Pt electrode was grounded.

TEM was used to investigate devices with different thicknesses before and after the application of consecutive low-voltage sweeps and high-voltage breakdown. Cross-sections from the Ag/GeTe/Pt devices were prepared using a dual-beam Helios NanoLab 650 (Thermo Fisher Scientific Inc.) scanning electron microscope. Before milling, a 1 µm-thick

© 2023 The Authors. Advanced Functional Materials published by Wiley-VCH GmbH

16163028, 0, Downloaded from https://onlinelibrary.wiley.com/doi/10.1002/adfm.202214615 by Tu Delft, Wiley Online Library on [01/05/2023]. See the Terms and Conditions (https://onlinelibrary.wiley.com/terms-and-conditions) on Wiley Online Library for rules of use; OA articles are governed by the applicable Creative Commons License

Pt protective layer was deposited on top of the Ag/GeTe/Pt device using electron- and ion-beam gas-assisted chemical vapor deposition. The TEM analysis was performed by operating the aberration-corrected Titan 80–300 (Thermo Fisher Scientific Inc.) transmission electron microscope in bright-field mode, with an accelerating voltage of 300 kV. Furthermore, dark-field scanning transmission electron microscopy (STEM), coupled with EELS, was performed for elemental analysis. Several images were captured at low and high magnifications, facilitating the imaging of the crystal structure and existing phases.

Supporting Information

Supporting Information is available from the Wiley Online Library or from the author.

Acknowledgements

This work was supported by Khalifa University of Science and Technology under award nos. 8474000134 and 21S104.

Conflict of Interest

The authors declare no conflict of interest.

Data Availability Statement

The data that support the findings of this study are available from the corresponding author upon reasonable request.

Keywords

germanium telluride (GeTe), germanium vacancies defects (V_{Ge}), PCM to RRAM interconversion, phase change memory, stopping voltage dependence

Received: December 14, 2022
Revised: February 12, 2023
Published online:

[1] R. S. Williams, *Comput. Sci. Eng.* **2017**, *19*, 7.
[2] K. J. Kuhn, *IEEE Trans. Electron Devices* **2012**, *59*, 1813.
[3] S. Salahuddin, S. Datta, *Nano Lett.* **2008**, *8*, 405.
[4] A. M. Ionescu, H. Riel, *Nature* **2011**, *479*, 329.
[5] a) H. J. Kim, D. S. Woo, S. M. Jin, H. J. Kwon, K. H. Kwon, D. W. Kim, D. H. Park, D. E. Kim, H. U. Jin, H. D. Choi, *Adv. Mater.* **2022**, *34*, 2203643; b) M. Ismail, C. Mahata, M. Kang, S. Kim, *Nanoscale Res. Lett.* **2022**, *17*, 61; c) A. Ali, H. Abbas, M. Hussain, S. H. A. Jaffery, S. Hussain, C. Choi, J. Jung, *Appl. Mater. Today* **2022**, *29*, 101554; d) A. Ali, H. Abbas, M. Hussain, S. H. A. Jaffery, S. Hussain, C. Choi, J. Jung, *Appl. Mater. Today* **2022**, *29*, 101554.
[6] a) A. Sebastian, M. Le Gallo, R. Khaddam-Aljameh, E. Eleftheriou, *Nat. Nanotechnol.* **2020**, *15*, 529; b) Y. Halawani, B. Mohammad, M. A. Lebdeh, M. Al-Qutayri, S. F. Al-Sarawi, *IEEE J. Emerg. Sel. Top. Circuits* **2019**, *9*, 388; c) H. Abunahla, B. Mohammad, D. Homouz, C. J. Okelly, *IEEE Trans. Circuits Syst.* **2016**, *63*, 2139.
[7] a) H. Abunahla, B. Mohammad, Y. Abbas, A. Alazzam, *Mater. Des.* **2021**, *210*, 110077; b) H. Abunahla, Y. Halawani, A. Alazzam, B. Mohammad, *Sci. Rep.* **2020**, *10*, 9473.
[8] a) T. Yamamoto, S. Hatayama, Y. Sutou, *Mater. Des.* **2022**, *216*, 110560; b) Y. T. Liu, X. B. Li, H. Zheng, N. K. Chen, X. P. Wang, X. L. Zhang, H. B. Sun, S. Zhang, *Adv. Funct. Mater.* **2021**, *31*, 2009803.
[9] A. S. Sokolov, H. Abbas, Y. Abbas, C. Choi, *J. Semicond.* **2021**, *42*, 013101.
[10] M. A. Lebdeh, H. Abunahla, B. Mohammad, M. Al-Qutayri, *IEEE Trans. Circuits Syst.* **2017**, *64*, 2427.
[11] a) W. Zhang, E. Ma, *Mater. Today* **2020**, *41*, 156; b) M. Salinga, B. Kersting, I. Ronneberger, V. P. Jonnalagadda, X. T. Vu, M. Le Gallo, I. Giannopoulos, O. Cojocaru-Mirédin, R. Mazzarello, A. Sebastian, *Nat. Mater.* **2018**, *17*, 681; c) S. Poddar, Y. Zhang, Y. Zhu, Q. Zhang, Z. Fan, *Nanoscale* **2021**, *13*, 6184; d) M. Ismail, C. Mahata, S. Kim, *J. Alloys Compd.* **2022**, *892*, 162141.
[12] a) M. E. Ketfi, H. Bennacer, S. S. Essaoud, M. I. Ziane, A. Boukortt, *Mater. Chem. Phys.* **2022**, *277*, 125553; b) K. Aryana, J. T. Gaskins, J. Nag, D. A. Stewart, Z. Bai, S. Mukhopadhyay, J. C. Read, D. H. Olson, E. R. Hoglund, J. M. Howe, *Nat. Commun.* **2021**, *12*, 774.
[13] a) Y. Trifonova, V. Ivanova, V. Lilova, D. Vasileva, T. Boteva, *J. Chem. Technol. Metall.* **2018**, *53*, 755; b) Y. Chen, H. Pan, S. Mu, G. Wang, R. Wang, X. Shen, J. Wang, S. Dai, T. Xu, *Acta Mater.* **2019**, *164*, 473; c) Y. Chen, H. Pan, S. Mu, G. Wang, R. Wang, X. Shen, J. Wang, S. Dai, T. Xu, *Acta Mater.* **2019**, *164*, 473.
[14] M. J. Yu, K. R. Son, A. C. Khot, D. Y. Kang, J. H. Sung, I. G. Jang, Y. D. Dange, T. D. Dongale, T. G. Kim, *J. Mater. Res. Technol.* **2021**, *15*, 1984.
[15] H. Y. Li, X. D. Huang, J. H. Yuan, Y. F. Lu, T. Q. Wan, Y. Li, K. H. Xue, Y. H. He, M. Xu, H. Tong, *Adv. Electron. Mater.* **2020**, *6*, 2000309.
[16] A. Velea, V. Dumitru, F. Sava, A.-C. Galca, C. Mihai, *Phys. Status Solidi RRL* **2021**, *15*, 2000475.
[17] K. A. Cooley, S. E. Mohney, *J. Vac. Sci. Technol., A* **2019**, *37*, 061510.
[18] A. Ali, S. M. Ansari, B. Ehab, B. Mohammad, D. H. Anjum, H. M. Aldosari, *Mater. Res. Bull.* **2022**, *146*, 111575.
[19] T. Chang, S.-H. Jo, W. Lu, *ACS Nano* **2011**, *5*, 7669.
[20] a) S. H. Jo, T. Chang, I. Ebong, B. B. Bhadviya, P. Mazumder, W. Lu, *Nano Lett.* **2010**, *10*, 1297; b) Y. Abbas, A. S. Sokolov, Y.-R. Jeon, S. Kim, B. Ku, C. Choi, *J. Alloys Compd.* **2018**, *759*, 44; c) S. Anwer, Y. Abbas, F. Ravaux, D. H. Anjum, Md. Rezeq, B. Mohammad, T. D. Dongale, K. Liao, W. Cantwell, D. Gan, *Appl. Mater. Today* **2022**, *29*, 101691.
[21] G. Modi, E. A. Stach, R. Agarwal, *ACS Nano* **2020**, *14*, 2162.
[22] Y. Jin, Y. Xiao, D. Wang, Z. Huang, Y. Qiu, L.-D. Zhao, *ACS Appl. Energy Mater.* **2019**, *2*, 7594.
[23] Y. Abbas, A. S. Sokolov, Y.-R. Jeon, S. Kim, B. Ku, C. Choi, *J. Alloys Compd.* **2018**, *759*, 44.
[24] Y. Abbas, Y.-R. Jeon, A. S. Sokolov, S. Kim, B. Ku, C. Choi, *Sci. Rep.* **2018**, *8*, 1228.
[25] a) M. Uenuma, Y. Ishikawa, Y. Uraoka, *Appl. Phys. Lett.* **2015**, *107*, 073503; b) P. Bousoulas, D. Sakellaropoulos, C. Papakonstantinop oulos, S. Kitsios, C. Arvanitis, E. Bagakis, D. Tsoukalas, *Nanotechnology* **2020**, *31*, 454002.
[26] A. Ali, Y. Abbas, H. Abbas, Y.-R. Jeon, S. Hussain, B. A. Naqvi, C. Choi, J. Jung, *Appl. Surf. Sci.* **2020**, *525*, 146390.
[27] a) Z. Liu, N. Sato, Q. Guo, W. Gao, T. Mori, *NPG Asia Mater.* **2020**, *12*, 66; b) A. H. Edwards, A. C. Pineda, P. A. Schultz, M. G. Martin, A. P. Thompson, H. P. Hjalmarson, *J. Phys.: Condens. Matter* **2005**, *17*, L329.
[28] a) V. Bragaglia, F. Arciprete, W. Zhang, A. M. Mio, E. Zallo, K. Perumal, A. Giussani, S. Cecchi, J. E. Boschker, H. Riechert, *Sci. Rep.* **2016**, *6*, 23843; b) T. Siegrist, P. Jost, H. Volker, M. Woda, P. Merkelbach, C. Schlockermann, M. Wuttig, *Nat. Mater.* **2011**, *10*, 202.
[29] a) S. Liu, W. Deng, in 2015 3rd IAPR Asian conference on pattern recognition (ACPR), IEEE, **2015**, pp. 730–734; b) X. Peng, R. Liu, S. Yu, 2019 IEEE International Symposium on Circuits and Systems (ISCAS), IEEE, **2019**, pp. 1–5.
[30] P.-Y. Chen, X. Peng, S. Yu, *IEEE Trans. Comput.* **2018**, *37*, 3067.

© 2023 The Authors. Advanced Functional Materials published by Wiley-VCH GmbH

16163028, 0, Downloaded from https://onlinelibrary.wiley.com/doi/10.1002/adfm.202214615 by Tu Delft, Wiley Online Library on [01/05/2023]. See the Terms and Conditions (https://onlinelibrary.wiley.com/terms-and-conditions) on Wiley Online Library for rules of use; OA articles are governed by the applicable Creative Commons License